A visual saliency-driven extraction framework of smoothly embedded entities in 3D point clouds of open terrain

Reuma Arav*, Sagi Filin*

Mapping and GeoInformation Engineering, Technion – Israel Institute of Technology, Haifa, Israel

Abstract

Three-dimensional documentation of natural and cultural geosites is gaining increasing attention as an indicative tool for environmental change. However, the entities therein pose a challenge to current extraction schemes due to their varying dimensions, complex shape, and most importantly, their seamless embedding in the surrounding topography. It is common to approach the extraction of these entities by developing landform-specific methods which are applied in a localized manner. Nonetheless, these methods hardly generalize, and different entities are dealt with independently, even when located at the same site. We propose in this paper a general, content-driven framework for the detection of smoothly embedded entities that, unlike prevalent approaches, seeks no specific form. We focus on salient entities, which attract visual attention within the point cloud and develop a new detection scheme, driven by homogeneity in the entities' saliency. We show how such formulation requires no approximate location or starting points and does not suffer from weak responses. Therefore, our framework can be readily applied to a multitude entities in various scenes, regardless of type or acquisition technique. We demonstrate our solution on airborne and terrestrial laser scans and detect entities of different types and shapes that feature in both natural and culturally-important sites. As we show, the proposed framework yields improved results compared to state-of-the-art counterparts.

Key words: Saliency, detection, embedded entities, 3D point clouds, geosites, variational methods

*Corresponding author

Email address: reumaa@technion.ac.il; reuma.arav@geo.tuwien.ac.at (Reuma Arav)

1. Introduction

Three-dimensional documentation of geosites, natural and heritage-related, is becoming a subject of greater attention because of their role as proxies for environmental change on the land (Sofia, 2020; Viles, 2016). The study of the entities therein presents a challenge to existing extraction schemes as the shape they wear is complex and does not conform to closed-parametric forms, they appear in varying dimensions, and more importantly they are embedded within the surrounding topography (Jaboyedoff and Derron, 2020; Oguchi, 2019; Telling et al., 2017). It is likely that for such reasons studies still resort to the manual delineation of objects of interest (e.g., Čeru et al., 2017; Kobiałka, 2018; Niculiţă et al., 2020; Peña-Villasenín et al., 2019). However, these analyses are limited in scope while repeated studies have proven that such a manner of extraction is prone to perception bias and degrades the detection accuracy (Hillier et al., 2014; Scheiber et al., 2015; Vinci et al., 2016).

To improve the detection performance, designated frameworks have been suggested, where entities are targeted based on prior knowledge of their shape characteristics at their study site. For example, Yu et al. (2015) utilized the flat surroundings of their study site to differentiate drumlins from their bases. Nenonen et al. (2018) applied a similar approach to inselbergs. The observation that moraines and liquefaction spread in a drumlin field share common orientation and dimensions has led Middleton et al. (2020) to create designated Gabor filter maps that are used in conjunction with curvature maps in a deep neural network. Such site-specific approaches are also prevalent in channel and gully detection. There, sink identification is followed by computation of flow accumulation and finalized by setting thresholds according to the features of interest (Dong et al., 2020; Stavi et al., 2018; Wu et al., 2018; Yang et al., 2018).

Detection in a more generalized manner, designed per entity but not per site, follows geomorphological characteristics and infers on points that belong to the feature of interest. As an example, Filin and Baruch (2010), and later on Rahimi and Alexander (2013), considered pit-like responses as sinkhole-related seeds and applied energy-based optimization to develop their boundaries. Wu et al. (2016) used the sinkhole concentric-contour forms to detect 1-m or deeper entities. Entity-based strategies are also prevalent in gully extraction schemes. Passalacqua et al. (2010) and Passalacqua et al. (2012) extracted gully thalwegs by utilizing flow accumulation and curvature measures as weights for the shortest path computation between two manually selected endpoints. Pelletier (2013) observed that gully-related points have higher contour curvature. Following the contour computation, high curvature valued regions were thinned into pixel-wide entities that were represented gullies. Xu et al. (2017) extracted gullies by differencing the normal and curvature values when computed by two different radii at each point. These were marked as gullies if their size surpassed a preset threshold. Additional applications that make use of localized and designated methods are found in abundance: Seers and Hodgetts (2016) extracted rock fractures and derived fracture network properties based on phase-congruency edge detection in image sequences; Djuricic et al. (2016) applied an openness index to extract oyster fossils, and Fanos et al. (2018), Mezaal and Pradhan (2018), and Mezaal et al. (2018) sought potential landslide zones by incorporating landslide-inventory rasters and slope, aspect, and curvature maps into hybrid machine learning (support vector machine and random forest) application. Geomorphometric features are also applied to reveal entities. As an example, Florinsky and Bliakharskii (2018) and Ishalina et al. (2021) searched for crevasses by using different curvature measures and texture variables. Pawłuszek et al. (2019) applied morphometric measures to map landslides in moderate relief agricultural regions, and ; Rahmati et al. (2019) used geomorphomteric variables and machine learning to predict snow avalanche hazards. Nonetheless, morphometric approaches tend to be entity-specific and rely on grid representation. This introduces biases and inaccuracies to the acquired point cloud (Florinsky, 2017). Lastly, an alternative framework that does seek specific entities applies change detection for geomorphological entity extraction (Anders et al., 2020; Hayakawa and Obanawa, 2020; Mayr et al., 2020; Williams et al., 2021). For example, Anders et al. (2020) recorded a sandy beach every hour for eleven days. After assessing the surface changes through time, the authors grouped neighboring locations that share similar change history. Such a framework requires sequential analysis, while the challenge of detecting entities within single epoch point clouds remains unsolved.

The variety of models and their specified nature allude to the complexity involved in entity extraction when embedded within open (non-urban) topography (Mayr et al., 2017; Roelens et al., 2018). Nonetheless, and as has been recently observed (Lague, 2020; Oguchi, 2019; Sofia, 2020), the development of more generalized frameworks is desirable, especially as the 3D documentation of geosites becomes a common practice. In this paper, we propose a novel approach for smoothly embedded entity extraction from 3D point clouds that is driven by content rather than by entity. Our approach requires no initialization or approximate locations as starting points. Additionally, it does not require a prerequisite training dataset and it does not suffer from weak responses that require additional algorithmic solutions for misidentifications. Our proposed model is based on the observation that the sought entities attract the visual attention within the point cloud and therefore can be regarded as locally salient. For their identification we develop a new measure that is not limited to small and confined point clouds and demonstrate its improved performance compared to state-of-the-art methods. In deriving the saliency measure we examine surface features suited for that purpose. We then test their application to our scheme and demonstrate that when curvature is concerned, a direct first-order evaluation by a non-parametric form performs better than more advanced forms. We then develop an optimality-driven detection solution, enabling the extraction of entities with smooth and continuous boundaries based on geometric homogeneity criteria. As the notion of saliency has never been utilized in such a framework (unlike gradients or curvature), we propose a model that can be integrated by a variational form. We demonstrate its applicability on two fundamentally different datasets: a dataset acquired by an airborne laser scanner that features different types of landforms; and a dataset acquired by a terrestrial laser scanner that captures a prehistoric formation composed of small stones that are fixated to a textured ground. We show that the proposed saliency metric marks entities of interest even in relatively smooth scenes while maintaining high performance and response to cluttered environments. Comparative analysis shows better performance in detection and extraction.

2. Methods

2.1. Detection and extraction framework

We consider visual saliency as a framework to localize on elements of interest and describe a variational extraction framework in which they are embedded. Later, we evaluate surface features that better reflect the notion of conspicuousness.

2.1.1. Salient entities

We seek to highlight smoothly embedded entities within the open terrain. The vague object-to-background transition (c.f. Dilo et al., 2007; Molenaar and Cheng, 2000; Stein et al., 2004, for this definition) suggests that direction-based methods are insufficiently sensitive to detect them. For that, we develop a saliency-driven approach. To define, visual saliency is an attentional mechanism that is based on the observation that neurons in the retina (center) are sensitive to regions that locally stand out from their surroundings and enables to focus the limited perceptual resources on pertinent subsets (Frintrop et al., 2010). Here, we seek a model that marks salient entities in point clouds of open terrain. To derive it we note that 3D point clouds are generally large and that the saliency estimation itself is only a preliminary stage. Therefore, our aim is to compute saliency with the least information required to generate a distinction. Our framework follows the center-surround notion (Abouelaziz et al., 2020; Itti et al., 1998; Wang et al., 2019) and develops an operator according to which distinctness is measured by the deviation of features in the area *surrounding* the point compared to the *center*. Our saliency metric is controlled by surface normals and curvature, where the local surface is defined by the neighborhood of a point and follows the center-surround principle, which seeks points with unique geometric attributes compared to their surrounding. A consideration when dealing with topography is that the surface varies continuously and smoothly. Therefore, uniqueness would not be reflected in the immediate nearby neighborhood, but rather in reference to farther regions. Accordingly, for the saliency metric computation, we lower the weights of nearby points while assigning higher ones to the surrounding regions. The weights assignment is dictated by a Gaussian-form-based radial function whose center is at ρ (minimal object size) and σ controls the breadth of the surrounding (Fig. 1).

$$w(x,y) = \frac{1}{\sqrt{2\pi}\sigma} \exp\left(-\frac{\left(\sqrt{x^2+y^2}-\rho\right)^2}{2\sigma^2}\right) \tag{1}$$

Under such setup, the center point would have a zero weight, while the maximal would be at ρ. Setting ρ and σ, and by using $w(x,y)$, we measure:

$$d\mathbf{n}(\mathbf{q}) = \frac{\iint_{\mathcal{S}} ||\mathbf{n}(\mathbf{q}) - \mathbf{n}(x,y)|| \cdot w(x,y) dxdy}{\iint_{\mathcal{S}} w(x,y) dxdy} \tag{2}$$

$$d\kappa(\mathbf{q}) = \frac{\iint_{\mathcal{S}} [\kappa(\mathbf{q}) - \kappa(x,y)] \cdot w(x,y) dxdy}{\iint_{\mathcal{S}} w(x,y) dxdy} \tag{3}$$

where $\mathbf{q}$ is the analyzed point, $\mathcal{S}$ is the surface such that $\mathcal{S}(x,y) : \mathbb{R}^2 \to \mathbb{R}$, $\mathbf{n}(\cdot)$ is the normal, $\kappa(\cdot)$ is the curvature, and $d\mathbf{n}$ and $d\kappa$ express the weighted mean difference between $\mathbf{q}$ and the surface for the normal and curvature, respectively. The value of $d\mathbf{n}$ is a function of the vector difference between $\mathbf{n}(\mathbf{q})$ and the surrounding normal directions $\mathbf{n}(x,y)$, reflecting the angular difference between the normal vectors. As an abundance of forms exist for defining both surface normal and curvature, we propose a set for their evaluation in Sec. (2.2). With the normalization of the two measures, the

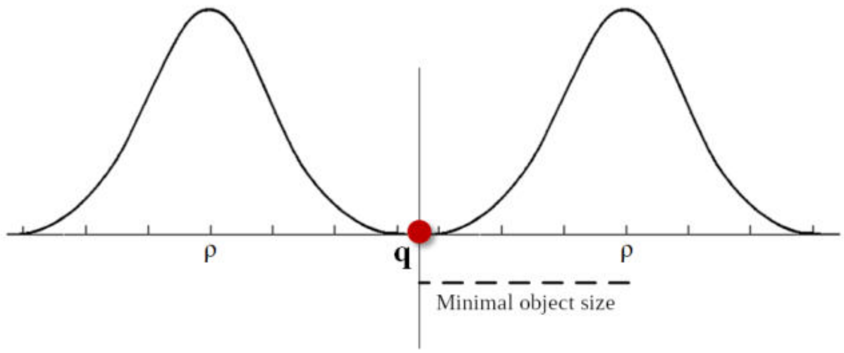

Figure 1: Weighting function for saliency detection: a center-surround filter that emphasizes regions at a distance ρ while suppressing closer and distant features.

saliency is given by:

$$S(\mathbf{q}) = 2 - [\exp(-d\mathbf{n}(\mathbf{q})) + \exp(-d\kappa(\mathbf{q}))] \tag{4}$$

where the exponents act as a normalization operator. Note that textured areas and noise are expressed in low variance by the saliency measures. Therefore, for each point, the variances of $d\mathbf{n}$ and $d\kappa$ are tested statistically using the χ^2-test. Statistically insignificant responses are marked as zero and are not considered in the overall saliency estimation.

2.1.2. Saliency-driven detection

To integrate the saliency map into an extraction framework, we seek boundaries that are continuous and smooth in shape and adhere to the edges of the salient region. The first two properties reflect our preference for simple forms, contrasting overly intricate ones, while the third reflects optimality of the boundary placement according to consistency principles that we outline in the following. To obtain these objectives, we formulate the extraction framework as an optimization problem such that the boundary quality can be quantified and targeted. The parametric energy-based models, such as the active-contour model, offer such a formulation. However, their application requires an initial estimate to secure convergence and the curve evolution requires reparametrization with each iteration. Moreover, given a set of curves, each curve is optimized independently and locally. Therefore, topological changes are not accommodated, and optimization is carried sequentially per curve.

For a more general approach, we develop a representation that operates directly on the data. For this, we use a level set formulation and turn it from a parametric representation of a curve into an implicit one. In such a form, a curve is regarded as the zero-level locus of an arbitrary, continuous, and smooth surface $\phi(\mathbf{x})$, where $\mathbf{x} = [x, y]$ are coordinates in a Euclidean frame. According to this representation, the surface is divided into three regions:

$$\phi(\mathbf{x}) = \begin{cases} \phi(\mathbf{x}) > 0 & \mathbf{x} \in \omega \\ \phi(\mathbf{x}) < 0 & \mathbf{x} \notin \omega \\ \phi(\mathbf{x}) = 0 & \mathbf{x} \in \mathcal{C} \end{cases}, \qquad \phi : \Omega \subset \mathbb{R}^2 \to \mathbb{R}. \tag{5}$$

where Ω is a 2-D domain. The surface is unimportant as our interest lies in the zero-level curve. Differing from the parametric contour evolution, here the surface is the one that evolves according to the internal and external forces, and the level set defines the contour form. In that respect, the geodesic active contour (GAC; Caselles et al., 1997) is considered the state-of-the-art. There, an equivalence of the active contour problem to a physical one is established such that the optimal curve is the path of least action (namely, the geodesic). By embedding the sought curve in a surface, the solution becomes the steady-state solution ($\phi_t = 0$) to the evolution equation:

$$\phi_t = g(I)\kappa + c \cdot g(I) + \nabla g(I) \nabla \phi \tag{6}$$

where c is a constant, $\kappa = \nabla \cdot \frac{\nabla \phi(\mathbf{x})}{|\nabla \phi(\mathbf{x})|}$ is the curvature of the embedded curve at point $\mathbf{x}$, I is the image, and $g(I)$ is an edge function. The first two terms in Eq. (6) are contour related, while the third is an external static force driven by the data. This formulation is advantageous on several counts: *i*) there is no need for advanced knowledge of the number of existing features and their whereabouts, suggesting that it allows topological change; *ii*) simultaneous evolutions rather than sequential one – unlike the active contours model, where each curve must be updated by its own, the parametric model updates all curves simultaneously as all curves are represented by a single surface; and *iii*) no need for reparametrization of the curve to arc-length at every iteration, as the surface updates in its entirety. However, we demonstrate that the application of this formulation to detect embedded entities is bound to fail from the start (Sec. 3). The reason is the smooth background-to-object transition, which is the main geometric characteristic of the embedded objects, which leads to weak edges. Specifically, it yields $g(I) \ll 1$, which translates to $\phi_t \to 0$, suggesting that the steady-state solution is reached from the onset. In the present case, the saliency defines objects whose boundaries are not defined by gradients. Therefore, the concept of gradients and edges cannot be cast here. Instead, we consider the saliency map as regions towards which boundaries we wish to attract the curves to, and as a solution framework we follow Chan and Vese (2001). Let $\bar{S}_{in}$, and $\bar{S}_{out}$ denote the mean saliency values of each region, and $|\mathcal{C}|$ the length of the curve $\mathcal{C}$, the energy functional is expressed by:

$$\begin{aligned} E(\mathcal{C}, \bar{S}_{in}, \bar{S}_{out}) = & \mu_1 \int_{inside(\mathcal{C})} \left|S(\mathbf{x}) - \bar{S}_{in}\right|^2 d\mathbf{x} \\ & + \mu_2 \int_{outside(\mathcal{C})} \left|S(\mathbf{x}) - \bar{S}_{out}\right|^2 d\mathbf{x} + \nu_0 \cdot |\mathcal{C}| \end{aligned} \tag{7}$$

where ν_0, μ_1, μ_2 are constant non-negative weighting scalars. This functional formulates the conditions for the curve we seek by means of a level-set function. The value of the energy $E(\mathcal{C}, \bar{S}_{in}, \bar{S}_{out})$ depends on the curve, and its minimum is achieved when the curve is optimal. The data terms $\left|S(\mathbf{x}) - \bar{S}_{in}\right|^2$ and $\left|S(\mathbf{x}) - \bar{S}_{out}\right|^2$ ensure the approximation to the saliency map, while the regularization term, $|\mathcal{C}|$, guarantees that the boundary between salient/non-salient regions has a minimal length. The statistic nature of this formulation, in the form of minimum variance, implies that no preliminary smoothing is needed. In essence, it also translates into little dependence on the curve initialization.

Solving this minimization problem through a level-set formulation requires defining the curve $\mathcal{C}$ as a function of the surface ϕ. For that we utilize the Heaviside function:

$$H(x) = \begin{cases} 1, & x \geq 0 \\ 0, & x < 0 \end{cases} , \tag{8}$$

as a means to define the interior ω. Similarly, we use $1 - H(x)$ to define the exterior, and the Dirac δ, such that $\frac{d}{dx}H(x) = \delta(x)$, to define the boundary itself. The energy equation then becomes:

$$\begin{aligned} E(\phi, \bar{S}_{in}, \bar{S}_{out}) = & + \mu_1 \int_{\Omega} \left|S(\mathbf{x}) - \bar{S}_{in}\right|^2 H(\phi(\mathbf{x})) d\mathbf{x} \\ & + \mu_2 \int_{\Omega} \left|S(\mathbf{x}) - \bar{S}_{out}\right|^2 (1 - H(\phi(\mathbf{x}))\, d\mathbf{x} + \nu_0 \int_{\Omega} \delta(\phi(\mathbf{x})) |\nabla \phi(\mathbf{x})| d\mathbf{x} \end{aligned} \tag{9}$$

with ϕ the embedding function. This functional is similar to Eq. (7), with the distinction that the energy is computed over the entire domain while the Heaviside function controls the influence of the "*inside*" and "*outside*" terms. The definition of the Heaviside function readily enables the computation of the mean saliency values inside and outside the curve:

$$\begin{aligned}\bar{S}_{in} &= \frac{\int_\Omega S(\mathbf{x})H(\phi)d\mathbf{x}}{\int_\Omega H(\phi)d\mathbf{x}} \\ \bar{S}_{out} &= \frac{\int_\Omega S(\mathbf{x})\left(1-H(\phi)\right)d\mathbf{x}}{\int_\Omega \left(1-H(\phi)\right)d\mathbf{x}}\end{aligned}. \tag{10}$$

Practically, regions where both the Heaviside function and the Dirac δ are zero will result in zero-motion, and will not propagate from the initial function. Instead, it is common to utilize a regularized form of both the Heaviside function and the Dirac δ, while upholding $\delta_\epsilon = H'_\epsilon(x)$:

$$H_\epsilon(x) = \frac{1}{2}\left[1 + \frac{2}{\pi}\arctan\left(\frac{x}{\epsilon}\right)\right] \tag{11}$$

and,

$$\delta_\epsilon(x) = H'_\epsilon(x) = \frac{1}{\pi}\cdot\frac{\epsilon}{\epsilon^2 + x^2}, \tag{12}$$

where ϵ is a small threshold. Keeping S_{in}, S_{out} fixed and minimizing Eq. (9) with respect to ϕ, we obtain the Euler-Lagrange equations for ϕ:

$$\phi_t = \delta(\phi)\left[-\mu_1\left[S(\mathbf{x}) - \bar{S}_{in}\right]^2 + \mu_2\left[S(\mathbf{x}) - \bar{S}_{out}\right]^2 + \nu_0\nabla\cdot\frac{\nabla\phi}{|\nabla\phi|}\right], \tag{13}$$

that define the evolution of the level-set function towards optimum, i.e., $\phi^{i+1} = \phi^{(i)} + \phi_t$, with i being the iteration index. One sees that Eq. (13) is of a region competition form: if the local saliency $S(\mathbf{x})$ at point $\mathbf{x}$ is more similar to the average of the interior, then $\mathbf{x}$ is assigned to the interior (the curve moves outwards) and vice versa. The solution is reached by the curves that are formed at the minimum when $\phi_t = 0$. As $\delta(\phi)$ reacts only at the level set, a rescaling is made by replacing $\delta(\phi)$ with $|\nabla\phi|$, which yields:

$$\phi_t = |\nabla\phi|\left[-\mu_1\left[S(\mathbf{x}) - \bar{S}_{in}\right]^2 + \mu_2\left[S(\mathbf{x}) - \bar{S}_{out}\right]^2 + \nu_0\nabla\cdot\frac{\nabla\phi}{|\nabla\phi|}\right]. \tag{14}$$

Whereas μ_1 and μ_2 control the smoothness of the curve, ν_0 sets its minimal length, measured by the dataset units. We use $\mu_1 = \mu_2 > 1$ and $\nu_0 > 0$ in all our computations. Note that the saliency is based on geometric properties of the surface, and therefore the model is still geometric.

2.2. Surface features

We describe the features used for computing the saliency measures, beginning with normal computation and turning to curvature. For surface normal computation we use the principal component analysis (PCA). Given a point $\mathbf{q}$ and its set of k neighbors $\mathbf{p}$, such that $\mathbf{p}_i \in \mathbf{p}$, we define $\bar{\mathbf{p}}_i = \mathbf{p}_i - \mathbf{q}$, and the covariance matrix, $\mathbf{C}$, by:

$$\mathbf{C} = \frac{1}{k}\sum_{i=1}^{k} \bar{\mathbf{p}}_i \cdot \bar{\mathbf{p}}_i^T\,; \quad \mathbf{C}\mathbf{v}_j = \lambda_j \mathbf{v}_j, \quad j \in \{1,2,3\} \tag{15}$$

where $\mathbf{v}_j$ and λ_j are the eigenvector and values, respectively. As $\mathbf{C}$ is positive semi-definite ($0 \leq \lambda_3 \leq \lambda_2 \leq \lambda_1$) we have $\mathbf{v}_3$, corresponding to λ_3, as the estimate of $\mathbf{n}^q$, the surface normal. We apply a closed-form solution to the third-degree characteristic polynomial for direct computation of the eigenvalues and henceforth of $\mathbf{v}_3$ (Appendix A). Notably, to disambiguate the normal sign, all normals are oriented toward a single viewpoint, v_p, such that:

$$\mathbf{n}^q = \begin{cases} \mathbf{n}^q, & \text{if } \mathbf{n}^q \cdot (\mathrm{v}_p - \mathbf{q}) \geq 0 \\ -\mathbf{n}^q, & \text{otherwise.} \end{cases} \tag{16}$$

By contrast, the estimation of surface curvature is more complex, due to its directionality and second-order form which exhibits a greater sensitivity to noise and surface texture. Among the different values, the two principal curvatures (the maximal and minimal) locally characterize the terrain, and according to Euler theorem, they facilitate the description of every other normal curvature value (Kreyszig, 1991). Even though immense literature has focused on their estimation in an unknown surface from point clouds, there is still no convention as to its estimation (e.g., Gois et al., 2006; Guerrero et al., 2018; Kalogerakis et al., 2009; Khameneifar and Ghorbani, 2018; Mérigot et al., 2011). Therefore, we consider three approaches: numerical, parametric, and non-parametric, with a focus on data characteristics, specifically noise and texture.

Numerical curvature estimation. Here, we utilize the Monge patch reparametrization, where $\mathcal{S} = [x, y, z(x,y)]$ (Kreyszig, 1991). Assuming that first-order derivatives of terrain features are relatively small, we approximate the principal curvature values by the eigenvalues of the Hessian matrix, $\mathbf{H}$, namely $\lambda_{\min,\max} \approx \kappa_{\min,\max}$, where λ and κ are the eigenvalues and curvature values, respectively. For a computationally efficient approach, adaptable to a variety of sizes, shapes, and forms, the approximation of the second-order derivatives of $\mathbf{H}$ is computed numerically. As the effect of noise and surface roughness may be documented within the curvature values, the response must be dominant enough. A lower response-level bound can be learned by examples or estimated theoretically by deriving an accuracy estimate σ_κ for the principal values. This is computed as a function of the range measurement accuracy, m_0 and by the minimal object response, ΔZ, defined by the terrain's surface roughness and relates to the curvature computation by $\varepsilon = 2\Delta Z/d^2$ where d is half the window size used for the numerical derivative estimation. Using propagation of variance, it can be shown the standard deviation of the eigenvalues, essentially of the principal curvature values, is $\sigma_\kappa = \pm m_0\sqrt{6}/d^2$. Assuming a normal distribution, i.e., $N \sim (\varepsilon, \sigma_\kappa)$, we establish a Z-test to determine if the computed curvature is statistically insignificant, meaning that only significant estimates are assigned a non-zero curvature value.

Parametric curvature estimation. For a parametric estimation we consider the bi-quadratic surface form that locally captures surface variation up to a second-order,

$$z(x,y) = \alpha_0 x^2 + \alpha_1 y^2 + \alpha_2 xy + \alpha_3 x + \alpha_4 y + \alpha_5 \tag{17}$$

where $\alpha_i, i \in \{0, 1, \ldots 5\}$ are the fitted bi-quadratic surface coefficients.[1] Since our interest lies only in the second-order term, and for computational efficiency, we transform the points in the neighborhood $\mathbf{p}$ to a local-horizon frame, thereby reducing the surface fitting to a three-parameter problem. Using $\mathbf{n}^q$, we compute the minimal rotation to transform the points to z-axis aligned normal direction. In such a form the axis of rotation is $\mathbf{t} = \mathcal{N}\left(\left[-n_y^q, n_x^q, 0\right]\right)^T$, where again $\mathcal{N}()$ is a normalization operator and the angle of rotation is $\theta = \cos^{-1}(n_z^q)$. Rotating the local normal so it points towards the global $z-$direction, we set $\mathbf{R} = n_z^q \cdot \mathbf{I} + \sqrt{1-(n_z^q)^2}[\mathbf{t}]_\times + (1-n_z^q)\left(\mathbf{t}\cdot\mathbf{t}^T\right)$, we have,

$$\mathbf{p}_{local}^q = \mathbf{R}\bar{\mathbf{p}}_i. \tag{18}$$

As the normal to the surface at $\mathbf{q}$ becomes $\mathbf{n}_{local}^q = [0,0,1]^T$, and since $\mathcal{S}_x \times \mathcal{S}_y = \mathbf{n}_{local}^q$, where $\mathcal{S}_x = [1,0,z_x]^T; \mathcal{S}_y = [0,1,z_y]^T$, we have that $z_x = z_y = 0$. Using Eq. (17) we can conclude that

[1] For a complete 3D point set, a local parametric form can be fitted using an implicit form (e.g., of a quadratic surface). If the quadratic surface is a sphere, the fitting reduces to a four-parameter linear estimation problem, but a sphere is limited in characterizing local curvature. A more global solution would involve an estimation of a fully quadratic surface which entails estimating ten parameters for each point.

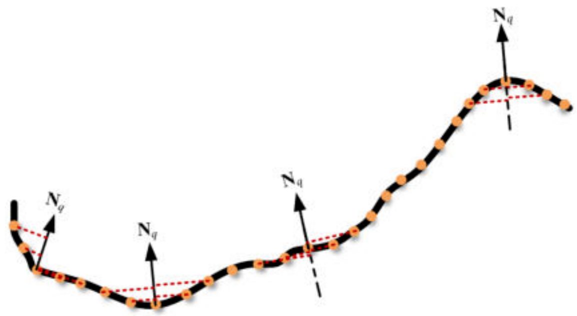

Figure 2: Convexity measure: the neighboring points are projected onto the center point normal direction $\mathbf{n}^q$.

$\alpha_3 = \alpha_4 = 0$, and consequently, the transformed neighborhood of $\mathbf{q}$ reduces the fitting problem to three parameters $(\alpha_0, \alpha_1, \alpha_2)$ instead of six. Through this approach, we simplify the computation of the principal curvature values to:

$$\kappa_{\text{min,max}} = \alpha_0 + \alpha_1 \pm \sqrt{(\alpha_0 + \alpha_1)^2 + \alpha_2^2}. \tag{19}$$

To ensure that the fitted surface is not flat, an F-test is used to evaluate if the adjusted coefficients $\alpha_0, \alpha_1, \alpha_2$ are statistically equal to zero. Note that as the test is for the planarity, no further tests are required to check that the curvature is significantly larger than the noise or roughness.

Non-parametric curvature estimation. Finally, the non-parametric approach is the simplest of the three and quantifies the convexity of the surface at each point by examining the characteristics of the points' distribution around it. To do so, we sum the projections of neighboring points on $\mathbf{n}^q$, and with that curvature is measured:

$$\kappa = \frac{1}{k} \sum_{i=1}^{k} \mathbf{n}^{q^T} \bar{\mathbf{p}}_i \tag{20}$$

Non-viable points, whose distribution around $\mathbf{q}$ is uneven, e.g., at the point cloud edges or near large areas of occlusions, are eliminated by projecting the neighborhood points to the tangent plane at $\mathbf{q}$, and analyzing the barycenter deviation from $\mathbf{q}$

$$d\mathbf{q} = \frac{1}{k} \sum_{i=1}^{k} \left(\mathbf{I} - \mathbf{n}^q \mathbf{n}^{q^T} \right) \bar{\mathbf{p}}_i \tag{21}$$

By contrast to the first two approaches, the noise and roughness effect on the curvature accuracy is estimated directly from the measurement accuracy, i.e., $\sigma_\kappa = m_0$. Similar to the numerical case, we use the Z-test to determine if a projection is a noise. This way, only significant projections are used for the non-parametric curvature estimation.

3. Results and Discussion

To evaluate the performance of our proposed detection framework we test it on airborne and terrestrial laser scans, where each dataset features entities at various dimensions, scales, forms, and densities. As our proposed model is point-based no preprocessing is required for the surface features and curvature computations. The model was implemented in Python 3.8, using Ubuntu 20.04 operating system on an 11th Gen Intel®Core™ i7 CPU@2.80GHz, with 16GB RAM.

Our quantitative evaluations of the extraction were performed in reference to manually delineated entities, which were extracted by a user not associated with the research. The detection results are classified into three categories: true-positive (TP), false-positive (FP), and false-negative (FN) (Xu et al., 2018). It is also customary to introduce another category of true-negative (TN) that relates to non-entities that are identified as such. In the present case, TN refers to all points in the scan where no detection was made, so that their quantification may bias the analysis and add irrelevant information. Therefore, they are left out of the analyses, and accordingly, common quality measures that consider false-negative detection (e.g., sensitivity, accuracy, etc.) are omitted as well. The three quality measures that utilized and relate to our classification categories are:

$$\begin{aligned} \text{precision} &= \frac{TP}{TP+FP}, \\ \text{recall} &= \frac{TP}{TP+FN} \\ \text{F1} &= 2 \cdot \frac{\text{precision} \cdot \text{recall}}{\text{precision} + \text{recall}} \end{aligned} \tag{22}$$

where *precision* quantifies the rate of identified TP for all positive results, *recall*, quantifies the percentage of correct detection in reference to ground-truth data, and the F1-test, also known as the *Sørensen-Dice coefficient*, that balances the precision and recall by computing their harmonic mean. As another metric, we use the Jaccard-index (mean Intersection over Union metric, IoU) to evaluate the delineation accuracy, which is defined by:

$$J(A,B) = \frac{1}{N}\sum_{i=1}^{N}\frac{|A \cap B|}{|A \cup B|} \tag{23}$$

with N the number of detected entities; A the coordinates of the automatically delineated polygon; and B the coordinates of the manually delineated one (Cortinhal et al., 2020).

3.1. Natural entity detection in airborne laser scans

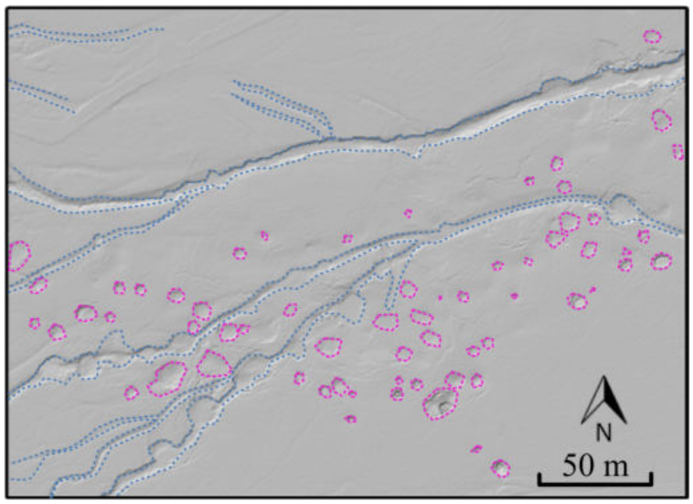

Figure 3: The alluvial fan dataset. A hillshaded depiction of the analyzed area, showing the intertwined gullies and sinkholes. This image is created from a 0.25 m grid DSM using the Natural Neighbor and Hillshade tools in ArcMap 10.1.

The first dataset is of the Ze'elim alluvial fan (lat. 31°22′, long. 35°24′), which lies along the Dead Sea coast and features a diverse set of geomorphic entities in different dimensions and forms (Fig. 3). Due to accelerated desiccation of the Dead Sea lake, at a rate that exceeds 1 m/yr level, the stability of the surrounding geomorphic system has been undermined, leading to a chain of reactions with disastrous effects on the natural environment. The more notable processes are the incisions of gullies and the accelerated development of sinkholes, the latter may form in large fields of 100 entities or more per site. Due to this rapid development and its hazardous nature, airborne scans are carried out on an annual basis to monitor such development (Arav et al., 2020). Our focus here is on an area of 300×250 m^2 within the fan that was scanned at a point density of 8 ± 3 pt/m^2. This section features two main gullies at widths of 5 and 9 m and depths ranging 2-6 m

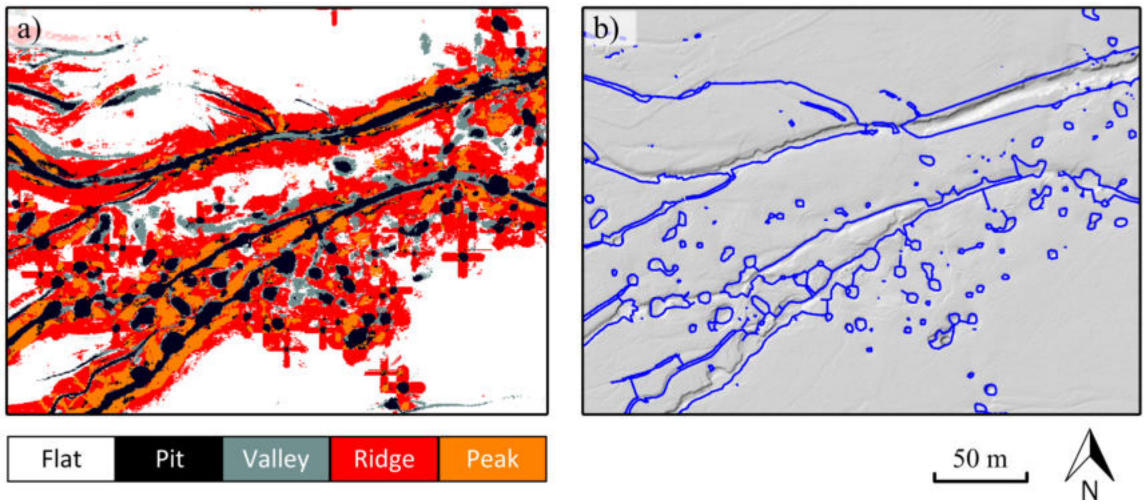

Figure 4: Surface classification and detection of dataset #2 based on Baruch (2011) model: a) classification; b) detection.

and three channels of 3 m wide and 0.5 m deep that fork from them. Additionally, 60 sinkholes are featured in the data, ranging from 0.5-4.5 m in depth, and 2-10 m in their radii.

Complete characterization in such complex environments is rare and usually focuses on a single entity, mostly detected using gradient-based methods that seek the breaklines they create in relatively homogeneous regions. However, the smooth transition, in this case, makes the applicability of such methods limited. Baruch (2011) developed a more general, multi-resolution, classification scheme which also accounts for measurement noise and surface texture. The classification of a point using this approach is according to its maximal responses among categories and resolutions. Application of the classification scheme to the Ze'elim dataset (Fig. 4a) shows that most gullies were classified as 'pit', rather than the expected 'valley'. Moreover, the banks of the gullies were classified either as ridges or as peaks. As this map is processed according to the classification, it leads to misclassification of entities.

Fig. (4b) shows the detection results when using the parametric-based snake evolution using the 'pit' map as an initialization phase. Note that as the evolution is carried per entity, a large portion of the gully banks was misidentified. As the curve is processed individually, it searches for the optimum based on the initial guess, which includes wrongful identifications. Quantitative analysis of the sinkhole detection shows a high F1-score value of 93%, as most sinkhole entities have been indeed identified. Nonetheless, the visual inspection demonstrates that the extraction is far from

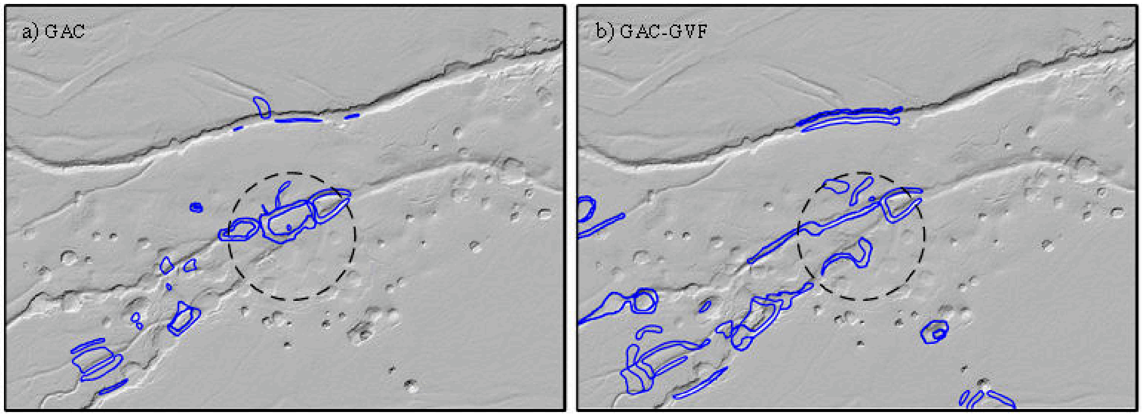

Figure 5: Result of GAC and a GAC-GVF on the alluvial fan dataset after 1500 iterations. The black dashed circle represents the initialization of the level-set contour: a) GAC application; b) an integration of GVF with GAC to enhance results.

satisfactory. The Jaccard-score is low (78%) as the detected boundary does not reach the correct rims or bank (having ridge-like properties). This dependence of the detection model on the initial classification processes highlights a key problem of such bottom-up schemes. It further stresses the need for direct detection.

In order to detect the entities regardless of class, we evaluate the performance of the classical geodesic active contour model (GAC, Eq. 6). We utilize the gradient-strength map (essentially a product of an edge map) as the driving force and initialize the level-set function at the center of the scan, closer to the southern gully. Fig. (5a) shows that the GAC has managed to expand towards the closest gully banks, but is mainly concentrated in the initial vicinity, with only a few curves farther away. To improve its performance, we integrated the gradient-vector-flow field (GVF) into the level-set form. Application of this form (Fig. 5b) has managed to drive the contours farther from the center, and to detect more of the gullies, yet leaving most entities undetected. In both forms, there are at least two contours for each entity: inside and outside the edge. Also, in both forms the forces are too weak to drive the detection farther than its initial shape. This is due to the weak gradients that surround the initial contour (essentially the fan surface) in conjunction with internal forces that confine the level-set to its initial area. These results may explain the need for initial seeds and the local expansion that follows (e.g., Baruch and Filin, 2011; Griffiths and Boehm, 2019). We conclude that the use of Eq. (6) alone has limited application in regions with homogeneous surroundings, also demonstrating the limitation of applying gradient-based solutions

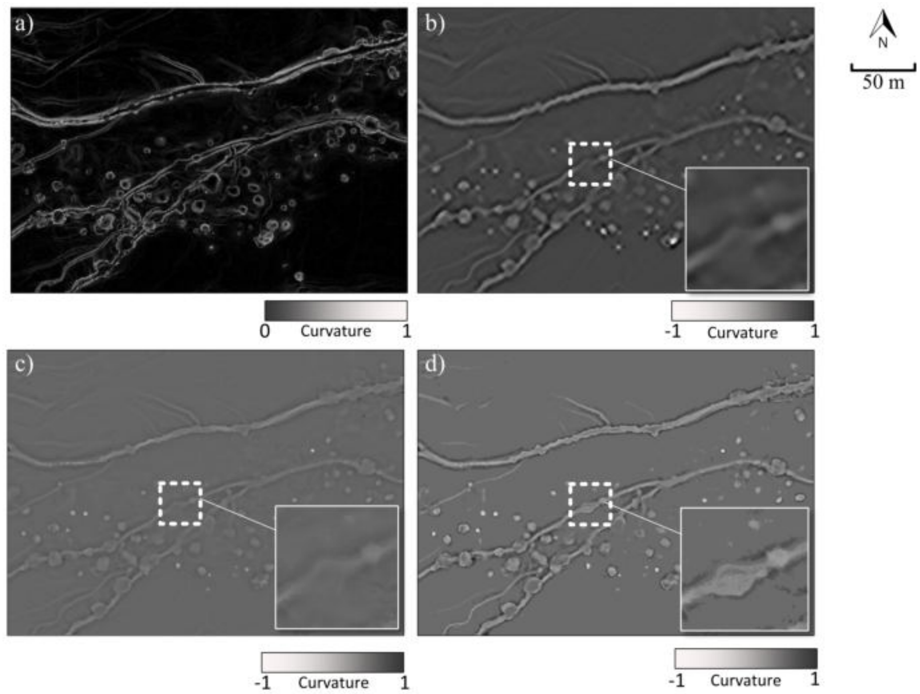

Figure 6: Normals and curvature maps. a) normal estimation with 1 m radius, represented as dip direction; b) numerical mean curvature with 5 m window; c) parametric mean curvature, with 4 m neighborhood radius; and d) non-parametric curvature, 4 m neighborhood radius. Note that shallower entities are more apparent in curvature maps than in the normal-based evaluation.

as a general framework to detect entities of this kind (e.g., Goodwin et al., 2016; Noto et al., 2017).

3.1.1. Evaluation of curvature computation methods

The introduction of curvature measures highlights the entities regardless of their depth (Fig. 6). While the normal-based evaluation emphasizes the entities' banks, the curvature highlights the entities. We test all three curvature estimation forms, with the parameters set following the minimal object size of ~2 m. Fig. (6) shows that all three measures have managed to identify the dominant entities within the scan. However, a more detailed inspection reveals that the non-parametric form has a more accurate characterization and better response for shallower entities (see focus boxes in Fig. 6b-c in comparison with Fig. 6d). This is because both numeric and parametric forms attempt to quantify a physical measure, either the eigenvalue or the second-order derivative. When the surrounding window for a point is inhomogeneous and mixes entity related points with ones in the surrounding region, the physical measures tend to underestimate the curvature related values. In contrast, the non-parametric form that requires a mere summation of the elevation differences with respect to the given point is unaffected and exhibits no sensitivity to this kind of distribution. As our evaluation is of entity related points concerning the surrounding region, the non-parametric form fairs better and becomes the preferable choice. This result is also evident when translating and incorporating the curvature measures into saliency maps (Fig. 7, column a). The addition of normals to the saliency estimation enables a better differentiation between entity and background, as the normals accentuate the banks. Notice that in the numeric and parametric estimations shallow sinkholes are not marked as salient. However, in the non-parametric estimation, shallow sinkholes, even those that lie within gullies, are marked as salient. The consequent detection responds to that fact (Fig. 7, column b). The non-parametric-based detection results in a more detailed characterization. More sinkholes and channels are identified while finer details of the gullies are better characterized (see arrows for specific examples). As the non-parametric curvature outperformed the other methods, we used its values to evaluate the proposed saliency measure.

3.1.2. Comparison of saliency computation methods

To compare our saliency measures, we tested them against common approaches. In the supplementary material a comparative evaluation for a watertight pointset is presented against point-based models proposed by Guo et al. (2018); Shtrom et al. (2013); Tasse et al. (2015), and in Sec. (3.2), a comparative evaluation against a terrestrial point cloud is given. Here, the span of the data over a wide region at a lower resolution than that of terrestrial or table scanners, has made point-based approaches difficult to apply. To generate comparative evaluations, we examined the application of two image-based saliency approaches proposed in Achanta et al. (2008, 2009). One is global in nature (Achanta et al., 2009), whereas the second is local (Achanta et al., 2008). The global approach estimates the saliency by:

$$\zeta(x, y) = |\bar{z}_\mu - \hat{z}_\sigma| \tag{24}$$

where $\bar{z}_\mu$ is the mean value of the elevations before Gaussian smoothing, and $\hat{z}_\sigma$ is a band-pass filtered version of the elevation map, computed by the difference of (Gaussian) smoothed elevation values, i.e., $\hat{z}_\sigma = z_{\sigma_1} - z_{\sigma_2}$, where the ratio of σ_1 and σ_2 is 1.6. The local approach computes the

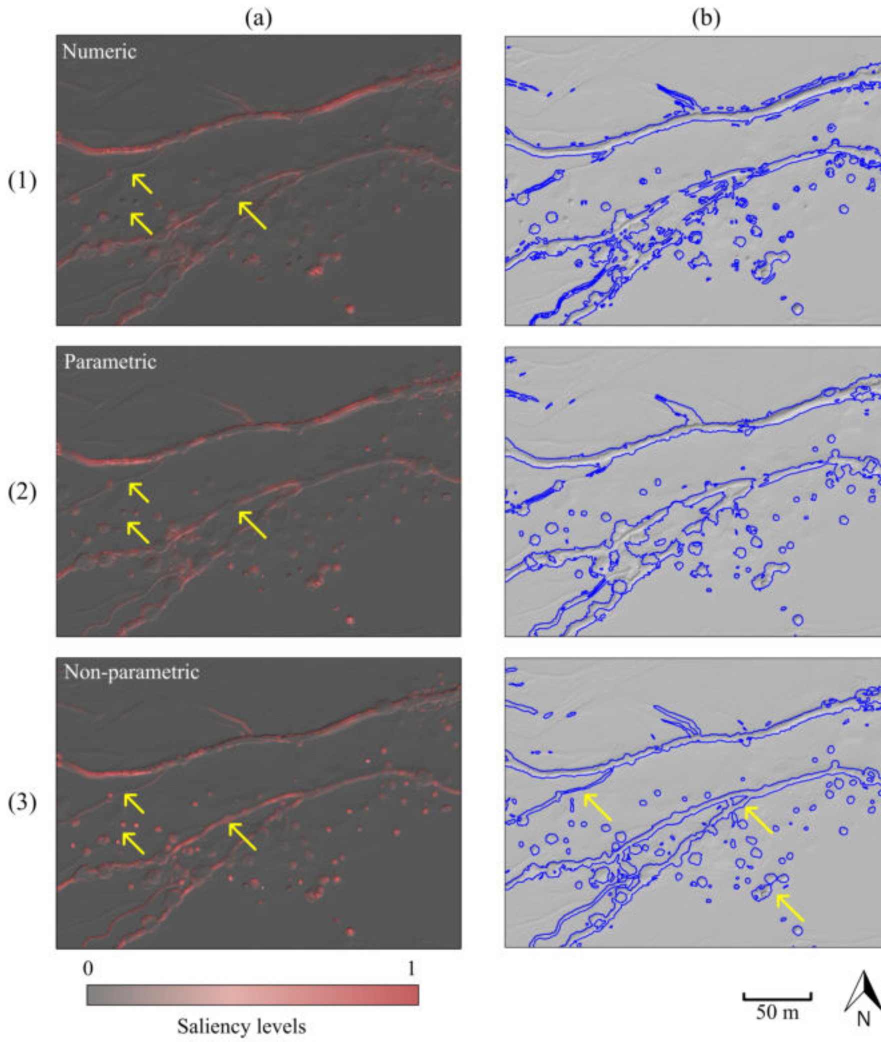

Figure 7: (a) Saliency estimations based on the different curvature evaluations. The arrows point to regions that are more salient in the non-parametric evaluation; (b) detection based on respective saliency maps. The arrows point to regions that are better characterized by the non-parametric based saliency.

saliency by local difference of sub-regions within the data, i.e.,

$$\zeta_{i,j} = D\left[\left(\frac{1}{N_1}\sum_{p=1}^{N_1} z_p\right), \left(\frac{1}{N_2}\sum_{q=1}^{N_2} z_q\right)\right] \tag{25}$$

where D is a Euclidean distance function; z_q, z_p are the elevation values; and N_1, N_2 are local neighborhoods.

Saliency maps based on each of these methods and the consequent detection are shown in Fig. (8.) The global approach, estimated here with four levels of σ (as proposed by the authors) results in emphasis on the eastern part on the fan and several sinkholes (Fig. 8a1). This can be attributed to their depth, as the saliency here is estimated according to features' elevation with respect to the global one. Deeper entities appear more salient than others. This fact is reaffirmed by the detection: deep sinkholes, as well as deeper parts of the gullies, attract the detection towards them and are extracted correctly (Fig. 8b1). Yet, the eastern part of the fan is detected as a separate region, due to some curvadness of the fan, which truly exists, but is not salient. This region overshadows the shallower entities within it, leaving many undetected.

The second row of Fig. (8) shows the saliency estimations using the local approach (Achanta et al., 2008). Here the saliency is estimated locally, based on small neighborhoods, making most gullies and sinkholes salient. However, clusters of sinkholes are detected as low saliency regions – since they are not salient compared to their immediate surrounding (see white arrows in col. (a)). The detection corresponds to that fact and shows that saliency-based extraction detects most entities in the scene. However, shallow parts that are close to deeper ones are not detected (yellow arrows). Our saliency measure (Sec. 2.1.1) applies a local concept, only instead of changes in depth, it measures the variation in both normal direction and curvature. Fig. 8 (third row) depicts the proposed saliency estimation and the detected entities using $\rho = 4$ m and $\sigma = 1.5$ m. Here, shallow entities are extracted, regardless of their neighboring features (yellow arrows). Note that the detection presented here is geometric in nature, as the saliency itself is computed according to both normals and convexity values. Additionally, the saliency measures are not binary by nature, but rather continuous. Therefore, they reflect locational vagueness, where no sharp boundaries exist (c.f., Dilo et al., 2007; Molenaar and Cheng, 2000; Stein et al., 2004) in the transition of the embedded features to the surrounding surface. In that respect, the detection phase seeks an optimal border in the mathematical/geometrical sense between two homogeneous groups: salient and non-

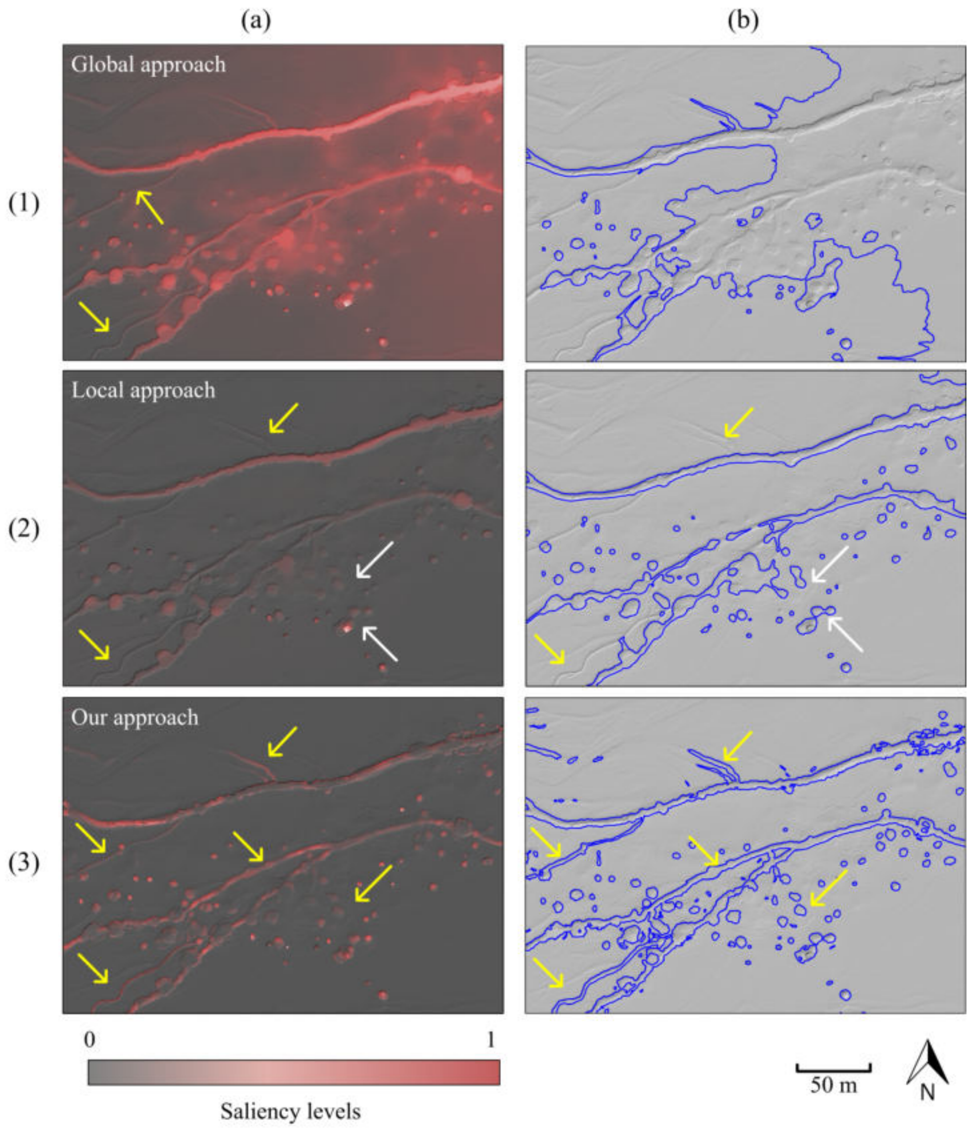

Figure 8: Entities extraction based on saliency estimations in the alluvial fan dataset: *Columns:* (a) saliency estimation; (b) detection using the proposed method. *Rows:*(1) saliency estimated according to global approach (Achanta et al., 2009) using $\sigma = \frac{1}{16}$ with four levels: $\sigma, 4\sigma, 6\sigma, \sigma$; (2) local approach (Achanta et al., 2008), with sub-region size of 5 m. White arrows mark examples of individual sinkholes that are detected as clusters; (3) proposed approach (Sec. 2.1.1), with $\rho = 4$ cm, $\sigma = 1.5$ m. The yellow arrows mark examples to shallow entities that are detected only by the proposed method.

salient. This homogeneity is computed as a deviation from each area's mean saliency value (Eq. 7), and thus may accommodates the vagueness. Finally, we note that the total computation time for

	Precision (%)	Recall (%)	F1 (%)	Jaccard (%)
Achanta et al. (2009) (global)	65	32	43	18
Achanta et al. (2008) (local)	85	84	84	66
Ours	**92**	**100**	**96**	**92**

Table 1: Performance analysis of different saliency estimations as the driving forces of the detection in the alluvial fan dataset. The global saliency estimation (Achanta et al., 2009) yielded the lowest F1-score of 43% and the lower Jaccard-index(18%). Overall, the F1-score and Jaccard-index of the proposed method were decidedly higher than the other methods (96% and 92%, respectively).

the saliency was 227 seconds. As the code was not optimized, faster runtime would be achieved without much effort. This can be useful for other downstream applications based on saliency, such as point cloud downsampling, registration, visualization, etc.

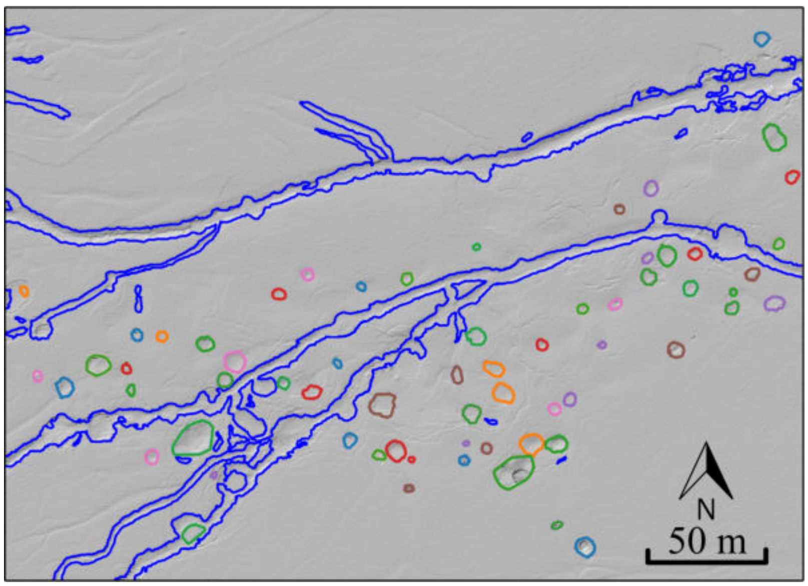

Figure 9: Detection results in the Ze'elim alluvial fan: detected gullies' banks are marked in blue, while sinkholes are colored. A recall of 100%, and precision of 92% due to false detection.

Fig. (9) shows the final detection results following the separation of sinkholes from gullies based on circularity (Appendix B), removal of shapes that lie within the boundaries of detected gullies, and filterization of small segments. Sixty sinkholes were correctly detected as individuals, while five local depressions were misidentified. The two dominant gullies were detected in full together with the three shallow channels.

Quantitative analysis shows 92% precision using the proposed saliency as region, compared to 85% and 65% based on the saliency estimations by Achanta et al. (2008) and Achanta et al. (2009), respectively (Table 1). The recall was lower, as false negatives were detected, which lead to F1-score of 96%. In comparison, the local approach by Achanta et al. (2009) reached an F1-score of 84%, while the global approach yielded only 43%. Notice that even though Achanta et al. (2008) achieved a high F1-score, the delineation accuracy described by the Jaccard-index was lower, reaching a mean value of 66% intersection over union. Here, again, the proposed method reached the highest score of 92%.

3.2. Cultural entity detection in terrestrial laser scans

In addition, we apply of the proposed method on point clouds that were acquired by a terrestrial laser scanner in an archaeological setting. Unlike airborne scans, terrestrially acquired point clouds document small-sized entities that may differ from the background only by a slight change in the geometry. Our evaluation is of an archaeological site, The Leopard Temple, located in the ‘Uvda Valley, Southern Israel (lat. $29°57'$, long. $34°58'$). The site, studied in the early 1980’s, is dated to 7500 BP (based on C^{14} evaluation) and is considered to have been in use for ~4000 years (Avner, 2002). In its vicinity lies a unique specimen of 16 animal-like figures, made of small stones affixed to the ground, and arranged along a 15 m stretch (Fig. 10). The figures were identified as leopards, due to their raised tails and the dark stones that symbolize their spots (Fig. 10a). One figure was identified as an antelope.

The site was scanned as part of a documentation campaign in the ‘Uvda Valley (Arav et al., 2016). Scans were acquired by the Leica c10 terrestrial laser scanner and because of technical limitations was measured only from a single position. The angular resolution was set to 0.1°, yielding a point cloud of 1,300,000 points, with an average point density of 40 ± 11 pts/cm^2 (Fig. 10b). The smallest stones are 1-3 cm long, with a 7 cm space between the stones. The larger stones are 10-30 cm long, positioned less than 4 cm apart. Most stones are no more than 2 cm above the ground, ranging up to 10 cm, with one reaching 20 cm above the ground. Here we focus on a characteristic detail from the entire site, which features 3-10 cm long stones, 1-5 cm high, and one exemption, $30 \times 20 \times 15$ cm stone (Fig. 11). Note, the terrain, though flat, is not smooth. The surface roughness, calculated by the standard deviation σ of the orthogonal residual distances of points to a fitted plane (Mills and Fotopoulos, 2013), was estimated as 0.01 m. This made the detection of the site stones a challenge (see also cross-section in Fig. 11).

Aiming to delineate the stones that compose the leopards and to autonomously produce a

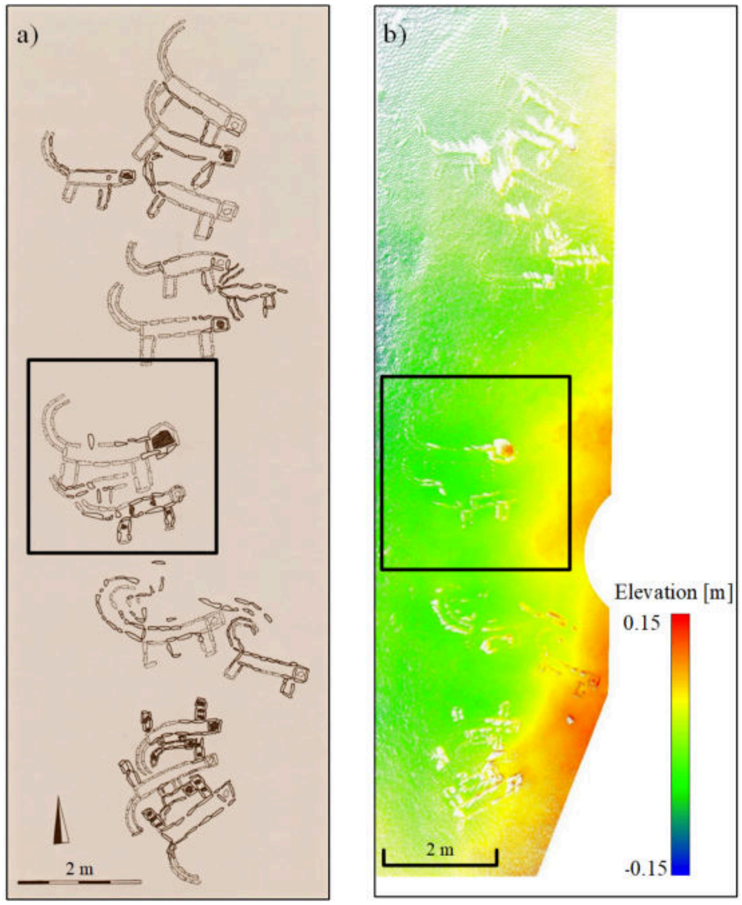

Figure 10: The Leopard Temple dataset: a) site map (with permission of Israel Antiquities Authority ©); b) scanned point cloud. Note the small differences in elevation, making the distinction between entity and background almost unnoticeable. The rectangle represents the analyzed region.

detailed map similar to that of Fig. (12a), we examine the application of energy-based models. First, we test the GAC with the embedded GVF model based on gradient maps. Fig. (12b) shows that only several of the larger stones were detected, though mostly inaccurately. As expected, the existing forces were insufficient to drive the curve much farther than its initial state. Trying to overcome the initialization phase, Filin and Baruch (2010), as well as Rahimi and Alexander (2013), proposed to first classify the data into geographic entities (i.e., flat, pit, peak ridge, and valley) using a multi-scale approach. Then, the active contour propagates from the convex-hull of the class of interest. Our detection concerns ridges since the stones that are laid upon the surface are similar to small ridges within the topography. However, it is noticeable that only large and

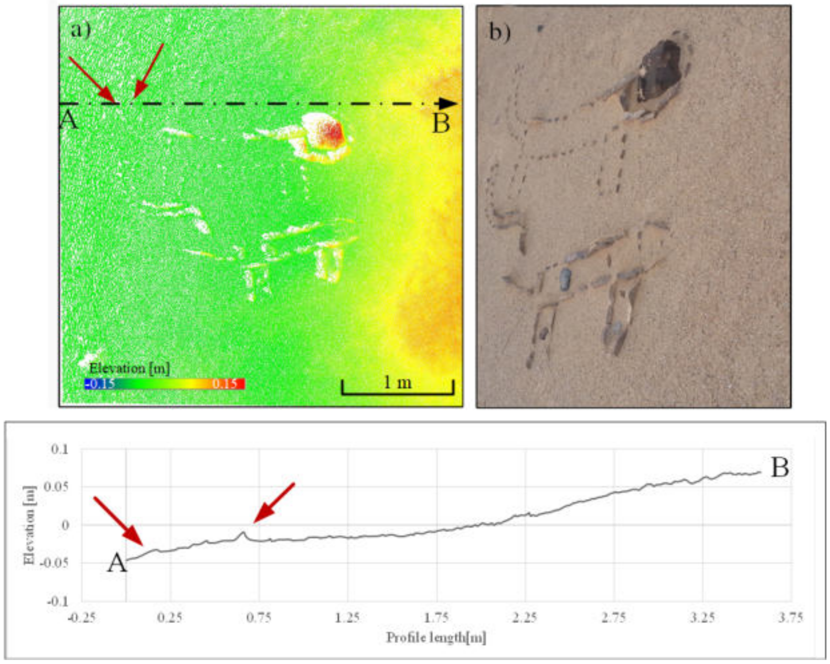

Figure 11: Detail of the Leopard Temple: a) a close look at the analyzed region; b) photograph focusing on the analyzed region; bottom: cross-section showing the elevation differences.

elongated stones are classified, leaving smaller stones out (Fig. 12c). This is a result of the scale-based classification which considers only strong responses in each scale. Though an improvement to the use of gradients, they are insufficient for a full description of the site, highlighting again the limitations of a bottom-up strategy.

Turning to saliency-based detection, Shtrom et al. (2013) proposed to measure global and local differences of features based on the uniqueness of normals in the immediate surrounding, while also assuming that salient regions make nearby areas salient. When this method is applied the stones' wider surrounding is emphasized, making it hard to distinguish, and consequently to delineate the details (Fig. 12d). Additionally, soil clods are also marked as salient, suggesting the existence of bigger entities than in reality. These results do not allow the construction of meaningful cues for accurate detection. Next, we evaluate our proposed saliency measures. As previously shown (Sec. 3.1), the non-parametric curvature fits better to the current application. Moreover, as the entities of interest are stones that form concave shapes on an approximately flat surface, and thus will respond better to the non-parametric curvature estimation, which essentially evaluates

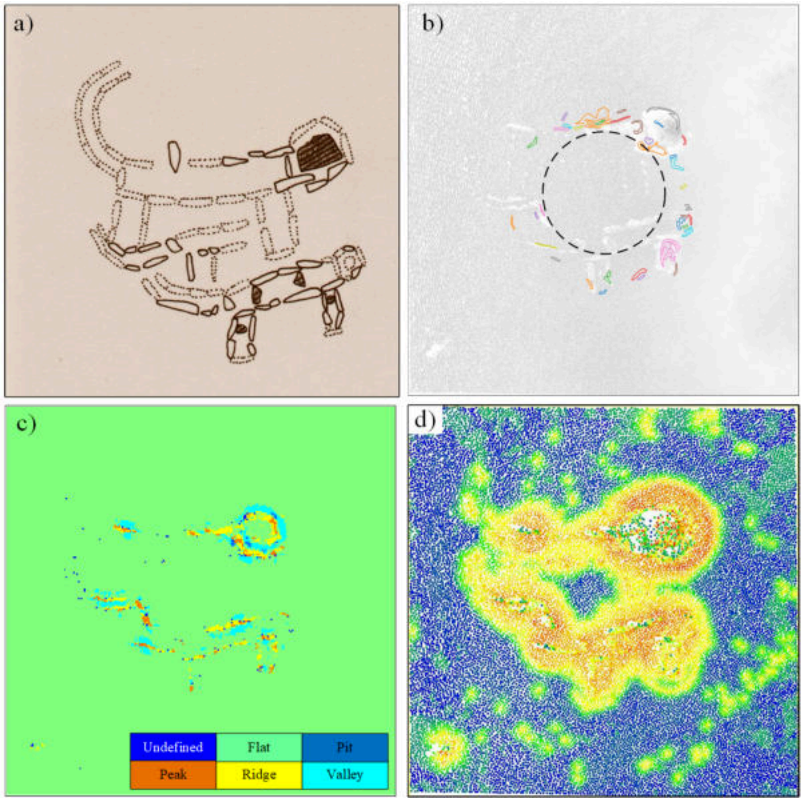

Figure 12: Application of state-of-the-art detection approaches to the Leopard Temple: a) detail from the site-map; b) application of GAC with embedded GVF, beginning from a circle at the middle of the point cloud; c) application of surface classification using Baruch (2011), roughness estimation set to 1 cm; d) application of saliency estimation as proposed by (Shtrom et al., 2013).

convexity. The neighborhood size is set to 3 cm, in accordance with the minimum object size. It should be noted that Shtrom et al. (2013) approach required 157 seconds to complete, while our approach needed only 33 seconds.

Aiming to examine the effect of surface roughness on curvature estimation, we first evaluated the curvature without attuning it to surface texture. This led to the modeling of the surface roughness and consequently, to the detection of soil clods (Fig. 13a-b). In order to assess the contribution of the curvature-based saliency to the detection, we used only curvature (Eq. 3) for the saliency estimation and consequent detection, at an effective distance of $\rho = 7$ cm (according to space between stones), and $\sigma = 2.3$ cm. We then applied the detection using the homogeneity criteria (Eq. 9). The results show that the saliency-based analysis eliminated some of the soil clods

(Fig. 13c-d). However, a few clods still remain, in addition to noisy contours and clusters of stones.

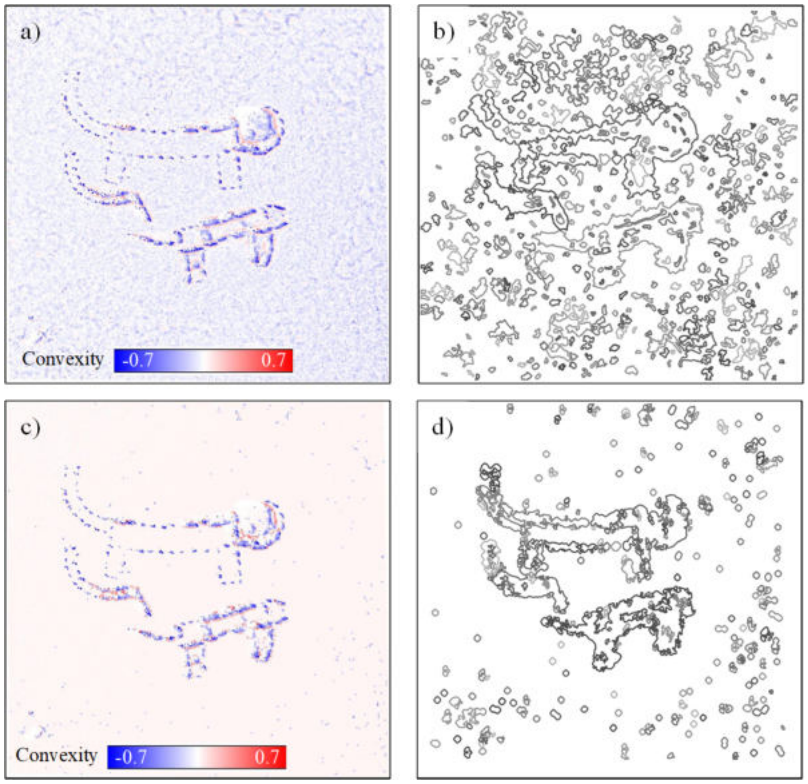

Figure 13: Non-parametric curvature computed with a neighborhood of 3 cm and consequent detection, using homogeneity criteria: a) non-parametric curvature estimation without roughness considerations and b) consequent detection based solely on curvature saliency; c) non-parametric curvature attuning for surface roughness, as proposed in Sec. (2.2); (d) consequent detection based solely on curvature saliency.

An addition of the normal-based saliency (Eq. 2) by using Eq. (4) yielded a result that emphasizes the leopard stones while suppressing ground-related regions (Fig. 14a). This is a direct result of the normal-based analysis. Since the normal changes only slightly at the presence of soil clods, it suppresses the salient signature produced by the change in curvature. Furthermore, the addition of normal-based saliency accentuates the boundaries of the stones so that a better separation between them is achieved. This response is similar to the one seen in the alluvial fan example (Fig. 7), where incorporating normals enabled a better characterization of fine details, highlighting the value of the proposed saliency map. The distinctness in relatively convex-wise homogeneous regions is improved by the combination of normal- and curvature-based saliency.

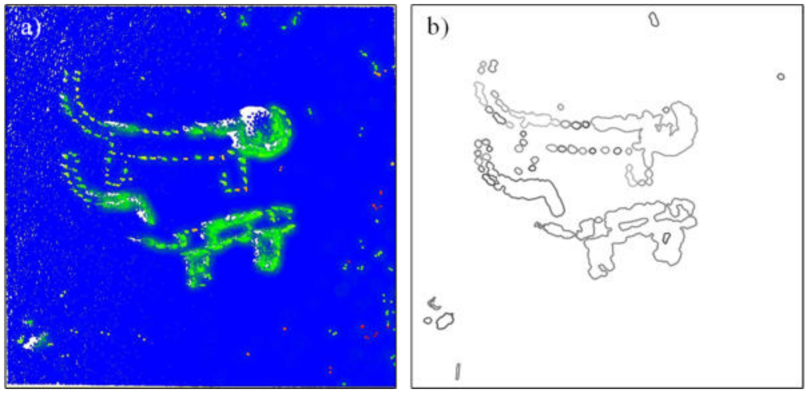

Figure 14: Saliency and detection results in the Leopard's Temple dataset: a) saliency-based on both normals and non-parametric curvature (with surface roughness considerations); and b) detection using the proposed method, setting the effective distance to 7 cm.

4. Conclusions

This paper presented a new method for visual saliency based detection model in 3D point clouds of open terrain. The proposed model, driven by homogeneity criteria, extracts a variety of smooth and continuous entities. Utilizing a new point-based visual saliency, which encapsulates geometric cues, we enable a direct extraction of entities from the data, without the need to reach optimal classification. We show that the proposed saliency measure marks regions of interest even in relatively smooth scenes while maintaining high performance and response to cluttered environments. Additionally, we evaluate the utility of numeric, parametric, and non-parametric methods for curvature computation, while analyzing their significance over surface texture. We show that of the three, the non-parametric representation of the surface, which involves only summation of the neighboring point projections, is most suited for saliency estimation.

Contrasting existing detection methods, the proposed model is not object-specified. It does not require an approximate initialization, a massive training dataset, or predefinition of geometric features. The extracted entities presented in this paper were acquired with different laser scanning techniques, wore linear and closed-shaped forms, have risen above the surface or laid below it, and were spread over a few centimeters or a few meters. All these point to the flexibility of the proposed model. Furthermore, results show localization of high level, which allows accurate detection of the phenomena borders, with a 92% Jaccard-score. The results show 96% F-1 score for detecting geomorphological entities. Compared to current variational detection models, our method facilitates a high extraction rate both in terrestrial and airborne scans of both natural and cultural entities with widths that range from a few centimeters to a few meters. Moreover, the scheme developed here was carried without imposing any shape constraints on the extracted contour shapes. Therefore, the application of the proposed method on other geomorphological entities, such as coastal dunes or snow landscapes, would be of interest in future research. Besides its direct application for detecting smoothly embedded and confined entities in open terrain, and as it requires no prior information for the extraction, the proposed method opens a new avenue for large scale detections, where it can be utilized as the initial engine to establish a labeled benchmark for complex entities in non-trivial applications.

References

Abouelaziz, I., Chetouani, A., Hassouni, M.E., Latecki, L.J., Cherifi, H., 2020. No-reference mesh visual quality assessment via ensemble of convolutional neural networks and compact multi-linear pooling. Pattern Recognition 100, 107174. doi:10.1016/j.patcog.2019.107174.

Achanta, R., Estrada, F., Wils, P., Süsstrunk, S., 2008. Salient region detection and segmentation. Computer Vision Systems , 66–75.

Achanta, R., Hemami, S., Estrada, F., Susstrunk, S., 2009. Frequency-tuned salient region detection, in: Computer vision and pattern recognition, 2009. cvpr 2009. ieee conference on, IEEE. pp. 1597–1604.

Anders, K., Winiwarter, L., Lindenbergh, R., Williams, J.G., Vos, S.E., Höfle, B., 2020. 4d objects-by-change: Spatiotemporal segmentation of geomorphic surface change from LiDAR time series. ISPRS Journal of Photogrammetry and Remote Sensing 159, 352–363. doi:10.1016/j.isprsjprs.2019.11.025.

Arav, R., Filin, S., Avner, U., Nadel, D., 2016. Three-dimensional documentation of masseboth sites in the ‘uvda valley area, southern negev, israel. Digital Applications in Archaeology and Cultural Heritage 3, 9–21. doi:10.1016/j.daach.2016.01.002.

Arav, R., Filin, S., Avni, Y., 2020. Sinkhole swarms from initiation to stabilisation based on in situ high-resolution 3-d observations. Geomorphology (submitted).

Avner, U., 2002. Studies in the Material and Spiritual Culture of the Negevand Sinai Populations, During the 6th-3rd Millennia B.C. Ph.D. thesis. The Hebrew University. Jerusalem.

Baruch, A., 2011. Characterization of Subtle Topographic Features Within Airborne Laser Scans. Ph.D. thesis. Technion-Israel Institute of Technology, Faculty of Civil and Environmental Engineering.

Baruch, A., Filin, S., 2011. Detection of gullies in roughly textured terrain using airborne laser scanning data. ISPRS Journal of Photogrammetry and Remote Sensing 66, 564–578. doi:10.1016/j.isprsjprs.2011.03.001.

Caselles, V., Kimmel, R., Sapiro, G., 1997. Geodesic Active Contours. International Journal of Computer Vision 22, 61–79. URL: http://link.springer.com/article/10.1023/A:1007979827043, doi:10.1023/A:1007979827043.

Čeru, T., Šegina, E., Gosar, A., 2017. Geomorphological dating of pleistocene conglomerates in central slovenia based on spatial analyses of dolines using LiDAR and ground penetrating radar. Remote Sensing 9, 1213. doi:10.3390/rs9121213.

Chan, T.F., Vese, L.A., 2001. Active contours without edges. IEEE Transactions on image processing 10, 266–277.

Cortinhal, T., Tzelepis, G., Aksoy, E.E., 2020. Salsanext: Fast, uncertainty-aware semantic segmentation of lidar point clouds for autonomous driving. arXiv preprint arXiv:2003.03653 .

Dilo, A., de By, R.A., Stein, A., 2007. A system of types and operators for handling vague spatial objects. International Journal of Geographical Information Science 21, 397–426. doi:10.1080/13658810601037096.

Djuricic, A., Dorninger, P., Nothegger, C., Harzhauser, M., Székely, B., Rasztovits, S., Mandic, O., Molnár, G., Pfeifer, N., 2016. High-resolution 3d surface modeling of a fossil oyster reef. Geosphere 12, 1457–1477.

Dong, P., Zhong, R., Xia, J., Tan, S., 2020. A semi-automated method for extracting channels and channel profiles from lidar-derived digital elevation models. Geosphere 16, 806–816. doi:10.1130/ges02188.1.

Fanos, A.M., Pradhan, B., Mansor, S., Yusoff, Z.M., bin Abdullah, A.F., 2018. A hybrid model using machine learning methods and GIS for potential rockfall source identification from airborne laser scanning data. Landslides 15, 1833–1850. doi:10.1007/s10346-018-0990-4.

Filin, S., Baruch, A., 2010. Detection of sinkhole hazards using airborne laser scanning data. Photogrammetric Engineering & Remote Sensing 76, 577–587. doi:10.14358/PERS.76.5.577.

Florinsky, I.V., 2017. An illustrated introduction to general geomorphometry. Progress in Physical Geography 41, 723–752. doi:10.1177/0309133317733667.

Florinsky, I.V., Bliakharskii, D., 2018. Crevasse detection by geomorphometric modelling of data from unmanned aerial survey, in: Popov, S., Gavrilkina, S., Pryakhina, G. (Eds.), Theory and Methods of Polar Science: Proceedings of International youth scientific conference on the polar geodesy, glaciology, hydrology, and geophysics, St. Petersburg, Russia. p. 280.

Frintrop, S., Rome, E., Christensen, H.I., 2010. Computational visual attention systems and their cognitive foundations. ACM Transactions on Applied Perception 7, 1–39. doi:10.1145/1658349.1658355.

Gois, J.P., Tejada, E., Etiene, T., Nonato, L.G., Castelo, A., Ertl, T., 2006. Curvature-driven modeling and rendering of point-based surfaces, in: 2006 19th Brazilian Symposium on Computer Graphics and Image Processing, IEEE. pp. 27–36.

Goodwin, N.R., Armston, J., Stiller, I., Muir, J., 2016. Assessing the repeatability of terrestrial laser scanning for monitoring gully topography: A case study from Aratula, Queensland, Australia. Geomorphology 262, 24–36. URL: https://www.sciencedirect.com/science/article/pii/S0169555X16300976, doi:10.1016/J.GEOMORPH.2016.03.007.

Griffiths, D., Boehm, J., 2019. Improving public data for building segmentation from convolutional neural networks (CNNs) for fused airborne lidar and image data using active contours. ISPRS Journal of Photogrammetry and Remote Sensing 154, 70–83. doi:10.1016/j.isprsjprs.2019.05.013.

Guerrero, P., Kleiman, Y., Ovsjanikov, M., Mitra, N.J., 2018. PCPNetLearning local shape properties from raw point clouds. Computer Graphics Forum 37, 75–85. doi:10.1111/cgf.13343.

Guo, Y., Wang, F., Xin, J., 2018. Point-wise saliency detection on 3D point clouds via covariance descriptors. Visual Computer 34, 1325–1338. doi:10.1007/s00371-017-1416-3.

Hayakawa, Y.S., Obanawa, H., 2020. Volumetric change detection in bedrock coastal cliffs using terrestrial laser scanning and UAS-based SfM. Sensors 20, 3403. doi:10.3390/s20123403.

Hillier, J.K., Smith, M.J., Armugam, R., Barr, I., Boston, C.M., Clark, C.D., Ely, J., Frankl, A., Greenwood, S.L., Gosselin, L., Hättestrand, C., Hogan, K., Hughes, A.L.C., Livingstone, S.J., Lovell, H., McHenry, M., Munoz, Y., Pellicer, X.M., Pellitero, R., Robb, C., Roberson, S., Ruther, D., Spagnolo, M., Standell, M., Stokes, C.R., Storrar, R., Tate, N.J., Wooldridge, K., 2014. Manual mapping of drumlins in synthetic landscapes to assess operator effectiveness. Journal of Maps 11, 719–729. URL: https://www.tandfonline.com/doi/full/10.1080/17445647.2014.957251, doi:10.1080/17445647.2014.957251.

Ishalina, O.T., Bliakharskii, D.P., Florinsky, I.V., 2021. Recognition of crevasses with high-resolution digital elevation models: Application of geomorphometric modeling and texture analysis. Transactions in GIS 25, 2529–2552. doi:10.1111/tgis.12790.

Itti, L., Koch, C., Niebur, E., 1998. A model of saliency-based visual attention for rapid scene analysis. IEEE Transactions on Pattern Analysis and Machine Intelligence 20, 1254–1259. doi:10.1109/34.730558.

Jaboyedoff, M., Derron, M.H., 2020. Landslide analysis using laser scanners, in: Developments in Earth Surface Processes. Elsevier, pp. 207–230. doi:10.1016/b978-0-444-64177-9.00007-2.

Kalogerakis, E., Nowrouzezahrai, D., Simari, P., Singh, K., 2009. Extracting lines of curvature from noisy point clouds. Computer-Aided Design 41, 282–292. doi:10.1016/j.cad.2008.12.004.

Khameneifar, F., Ghorbani, H., 2018. On the curvature estimation for noisy point cloud data via local quadric surface fitting. Computer-Aided Design and Applications 16, 140–149. doi:10.14733/cadaps.2019.140-149.

Kobiałka, D., 2018. Living monuments of the second world war: Terrestrial laser scanning and trees with carvings. International Journal of Historical Archaeology 23, 129–152. doi:10.1007/s10761-018-0462-5.

Kopp, J., 2008. Efficient numerical diagonalization of Hermitian 3×3 matrices. International Journal of Modern Physics C 19, 523–548. doi:10.1142/s0129183108012303.

Kreyszig, E., 1991. Differential Geometry. Dover Books on Mathematics. 1st ed., Dover Publications. URL: http://gen.lib.rus.ec/book/index.php?md5=88CA1CD6A9999A5ACA3C2E3566E84900.

Lague, D., 2020. Terrestrial laser scanner applied to fluvial geomorphology, in: Developments in Earth Surface Processes. Elsevier, pp. 231–254. doi:10.1016/b978-0-444-64177-9.00008-4.

Mayr, A., Bremer, M., Rutzinger, M., 2020. 3D Point errors and change detection accuracy of unmanned aerial vehicle laser scanning data. ISPRS Annals of Photogrammetry, Remote Sensing and Spatial Information Sciences V-2-2020, 765–772. doi:10.5194/isprs-annals-v-2-2020-765-2020.

Mayr, A., Rutzinger, M., Bremer, M., Oude Elberink, S., Stumpf, F., Geitner, C., 2017. Object-based classification of terrestrial laser scanning point clouds for landslide monitoring. The Photogrammetric Record 32, 377–397. URL: https://onlinelibrary.wiley.com/doi/abs/10.1111/phor.12215, doi:10.1111/phor.12215, arXiv:https://onlinelibrary.wiley.com/doi/pdf/10.1111/phor.12215.

Mérigot, Q., Ovsjanikov, M., Guibas, L.J., 2011. Voronoi-based curvature and feature estimation from point clouds. IEEE Transactions on Visualization and Computer Graphics 17, 743–756. doi:10.1109/tvcg.2010.261.

Mezaal, M., Pradhan, B., Rizeei, H., 2018. Improving landslide detection from airborne laser scanning data using optimized dempster–shafer. Remote Sensing 10, 1029. doi:10.3390/rs10071029.

Mezaal, M.R., Pradhan, B., 2018. An improved algorithm for identifying shallow and deep-seated landslides in dense tropical forest from airborne laser scanning data. CATENA 167, 147–159. doi:10.1016/j.catena.2018.04.038.

Middleton, M., Heikkonen, J., Nevalainen, P., Hyvönen, E., Sutinen, R., 2020. Machine learning-based mapping of micro-topographic earthquake-induced paleo-pulju moraines and liquefaction spreads from a digital elevation model acquired through laser scanning. Geomorphology 358, 107099. doi:10.1016/j.geomorph.2020.107099.

Mills, G., Fotopoulos, G., 2013. On the estimation of geological surface roughness from terrestrial laser scanner point clouds 9, 1410–1416. doi:10.1130/ges00918.1.

Molenaar, M., Cheng, T., 2000. Fuzzy spatial objects and their dynamics. ISPRS Journal of Photogrammetry and Remote Sensing 55, 164–175. doi:10.1016/s0924-2716(00)00017-4.

Nenonen, K., Johansson, P., Sallasmaa, O., Sarala, P., Palmu, J.P., 2018. The inselberg landscape in finnish lapland: a morphological study based on the LiDAR data interpretation. Bulletin of the Geological Society of Finland 90, 239–256. doi:10.17741/bgsf/90.2.008.

Niculiţă, M., Mărgărint, M.C., Tarolli, P., 2020. Using UAV and LiDAR data for gully geomorphic changes monitoring, in: Developments in Earth Surface Processes. Elsevier, pp. 271–315. doi:10.1016/b978-0-444-64177-9.00010-2.

Noto, L.V., Bastola, S., Dialynas, Y.G., Arnone, E., Bras, R.L., 2017. Integration of fuzzy logic and image analysis for the detection of gullies in the calhoun critical zone observatory using airborne LiDAR data. ISPRS Journal of Photogrammetry and Remote Sensing 126, 209–224. doi:10.1016/j.isprsjprs.2017.02.013.

Oguchi, T., 2019. Geomorphological mapping based on DEMs and GIS: A review. Abstracts of the ICA 1, 1–1. doi:10.5194/ica-abs-1-275-2019.

Passalacqua, P., Belmont, P., Foufoula-Georgiou, E., 2012. Automatic geomorphic feature extraction from lidar in flat and engineered landscapes. Water Resources Research 48. URL: http://dx.doi.org/10.1029/2011WR010958, doi:10.1029/2011WR010958.

Passalacqua, P., Do Trung, T., Foufoula-Georgiou, E., Sapiro, G., Dietrich, W.E., 2010. A geometric framework for channel network extraction from lidar: Nonlinear diffusion and geodesic paths. Journal of Geophysical Research: Earth Surface 115. URL: http://dx.doi.org/10.1029/2009JF001254, doi:10.1029/2009JF001254.

Pawłuszek, K., Marczak, S., Borkowski, A., Tarolli, P., 2019. Multi-aspect analysis of object-oriented landslide detection based on an extended set of LiDAR-derived terrain features. ISPRS International Journal of Geo-Information 8, 321. doi:10.3390/ijgi8080321.

Pelletier, J.D., 2013. A robust, two-parameter method for the extraction of drainage networks from high-resolution digital elevation models (DEMs): Evaluation using synthetic and real-world DEMs. Water Resources Research 49, 75–89. doi:10.1029/2012wr012452.

Peña-Villasenín, S., Gil-Docampo, M., Ortiz-Sanz, J., 2019. Professional SfM and TLS vs a simple SfM photogrammetry for 3d modelling of rock art and radiance scaling shading in engraving detection. Journal of Cultural Heritage 37, 238–246. doi:10.1016/j.culher.2018.10.009.

Rahimi, M., Alexander, E.C.J., 2013. Locating sinkholes in LiDAR coverage of a glacio-fluvial karst, Winona County, mn, in: Smith, B.A., Hunt, B.B. (Eds.), 13th Sinkhole Conference, Carlsbad, New Mexico, USA.

Rahmati, O., Ghorbanzadeh, O., Teimurian, T., Mohammadi, F., Tiefenbacher, J.P., Falah, F., Pirasteh, S., Ngo, P.T.T., Bui, D.T., 2019. Spatial modeling of snow avalanche using machine learning models and geo-environmental factors: Comparison of effectiveness in two mountain regions. Remote Sensing 11, 2995. doi:10.3390/rs11242995.

Roelens, J., Höfle, B., Dondeyne, S., Van Orshoven, J., Diels, J., 2018. Drainage ditch extraction from airborne lidar point clouds. ISPRS Journal of Photogrammetry and Remote Sensing 146, 409 – 420. URL: http://www.sciencedirect.com/science/article/pii/S0924271618302922, doi:https://doi.org/10.1016/j.isprsjprs.2018.10.014.

Scheiber, T., Fredin, O., Viola, G., Jarna, A., Gasser, D., Łapińska-Viola, R., 2015. Manual extraction of bedrock lineaments from high-resolution LiDAR data: methodological bias and human perception. GFF 137, 362–372. URL: http://www.tandfonline.com/doi/full/10.1080/11035897.2015.1085434, doi:10.1080/11035897.2015.1085434.

Seers, T.D., Hodgetts, D., 2016. Extraction of three-dimensional fracture trace maps from calibrated image sequences. Geosphere 12, 1323–1340. doi:10.1130/ges01276.1.

Shtrom, E., Leifman, G., Tal, A., 2013. Saliency Detection in Large Point Sets, in: Computer Vision (ICCV), 2013 IEEE International Conference on, pp. 3591–3598. doi:10.1109/ICCV.2013.446.

Sofia, G., 2020. Combining geomorphometry, feature extraction techniques and earth-surface processes research: The way forward. Geomorphology 355, 107055. doi:10.1016/j.geomorph.2020.107055.

Stavi, I., Chocron, M., Filin, S., Arav, R., Ackermann, O., Zissu, B., 2018. Intentional, dual purpose of ancient wine presses as cisterns for runoff water harvesting in drylands. The Holocene 28, 1107–1112. doi:10.1177/0959683618761550.

Stein, A., Dilo, A., Lucieer, A., van de Vlag, D., Van De, D., 2004. Definition and identification of vague spatial objects and their use in decision ontologies. ISSDQ 04, Bruck ad Leitha, Department of Geoinformation and Cartography .

Tasse, P.F., Kosinka, J., Dodgson, N., 2015. Cluster-based point set saliency, in: Proceedings of the IEEE international conference on computer vision, pp. 163–171.

Telling, J., Lyda, A., Hartzell, P., Glennie, C., 2017. Review of earth science research using terrestrial laser scanning. Earth-Science Reviews 169, 35–68. doi:10.1016/j.earscirev.2017.04.007.

Viles, H., 2016. Technology and geomorphology: Are improvements in data collection techniques transforming geomorphic science? Geomorphology 270, 121–133. doi:10.1016/j.geomorph.2016.07.011.

Vinci, A., Todisco, F., Mannocchi, F., 2016. Calibration of manual measurements of rills using Terrestrial Laser Scanning. CATENA 140, 164–168. URL: https://www.sciencedirect.com/science/article/pii/S034181621630042X, doi:10.1016/J.CATENA.2016.01.026.

Wang, W., Shen, J., Xie, J., Cheng, M.M., Ling, H., Borji, A., 2019. Revisiting video saliency prediction in the deep learning era. IEEE Transactions on Pattern Analysis and Machine Intelligence , 1–1doi:10.1109/tpami.2019.2924417.

Williams, J.G., Anders, K., Winiwarter, L., Zahs, V., Höfle, B., 2021. Multi-directional change detection between point clouds. ISPRS Journal of Photogrammetry and Remote Sensing 172, 95–113. doi:10.1016/j.isprsjprs.2020.12.002.

Wu, H., Xu, X., Zheng, F., Qin, C., He, X., 2018. Gully morphological characteristics in the loess hilly-gully region based on 3d laser scanning technique. Earth Surface Processes and Landforms 43, 1701–1710. doi:10.1002/esp.4332.

Wu, Q., Deng, C., Chen, Z., 2016. Automated delineation of karst sinkholes from LiDAR-derived digital elevation models. Geomorphology 266, 1–10. doi:10.1016/j.geomorph.2016.05.006.

Xu, Y., Tuttas, S., Hoegner, L., Stilla, U., 2018. Voxel-based segmentation of 3d point clouds from construction sites using a probabilistic connectivity model. Pattern Recognition Letters 102, 67–74. doi:10.1016/j.patrec.2017.12.016.

Xu, Y., Yue, D., He, P., 2017. Point cloud segmentation of gully based on characteristic difference using airborne lidar data. ISPRS - International Archives of the Photogrammetry, Remote Sensing and Spatial Information Sciences XLII-2/W7, 307–311. doi:10.5194/isprs-archives-xlii-2-w7-307-2017.

Yang, X., Na, J., Tang, G., Wang, T., Zhu, A., 2018. Bank gully extraction from DEMs utilizing the geomorphologic features of a loess hilly area in china. Frontiers of Earth Science 13, 151–168. doi:10.1007/s11707-018-0700-5.

Yu, P., Eyles, N., Sookhan, S., 2015. Automated drumlin shape and volume estimation using high resolution LiDAR imagery (curvature based relief separation): A test from the wadena drumlin field, minnesota. Geomorphology 246, 589–601. doi:10.1016/j.geomorph.2015.07.020.

Appendix A. Direct computation of surface normal

We take advantage of the fact that a closed form solution exists to the third degree characteristic polynomial, and instead of applying a general computation of the roots, we compute the eigenvalues as follows (Kopp, 2008):

$$\begin{aligned} \lambda_1 &= \mu + 2\nu \cdot \cos\theta \\ \lambda_2 &= \mu + 2\nu \cdot \cos(\theta + 120^\circ) \\ \lambda_3 &= 3\mu - \lambda_1 - \lambda_2 \end{aligned} \tag{A.1}$$

where:

$$\begin{aligned} \mu &= \frac{1}{3} tr(\mathbf{C}) \\ \nu &= \sqrt{\frac{tr\left((\mu \cdot \mathbf{I} - \mathbf{C})^2\right)}{6}} \\ \theta &= \frac{1}{3}\cos^{-1}\left(\det\left(\frac{\mathbf{C} - \mu\mathbf{I}}{2\nu}\right)\right) \end{aligned} \tag{A.2}$$

and $\mathbf{I}$ is a 3×3 identity matrix. As our interest is only in $\mathbf{v}_3$, we compute it directly as the cross-product between two rows of $\mathbf{C} - \lambda_3\mathbf{I}$, further reducing the runtime. The small set of computations readily lends itself to parallel computation of the normals for the whole point set, as was done in the present case.

Appendix B. Separation of sinkholes from gullies

To signal out sinkholes we follow Filin and Baruch (2010), who proposed simple and efficient measures to reflect the circular 2-D shape and the concave 3-D form of the sinkholes, with respect to the surrounding surface. Each of the extracted contours is evaluated according to the entrapped area (A) and the shape compactness (C),

$$A = \frac{1}{2}\left\|\sum_{i=1}^{n} x_i\left(y_{i+1} - y_{i-1}\right)\right\| \tag{B.1}$$

$$C = \frac{\ell^2}{4\pi A} \tag{B.2}$$

with n the number of boundary points; x_i, y_i, their coordinates; and ℓ, the perimeter. The area evaluation ensures that contours did not collapse unto themselves. Boundary and compactness measures similarity (and deviation) of the outer shape to circular form, which sinkholes tend to exhibit. The 3-D shape is evaluated by analyzing how detected sinkholes are embedded in their surroundings. This test is performed by fitting a local bi-quadratic surface (Eq. 17) to the points surrounding the sinkhole and comparing the relative depth of each inner point to the adjusted surface. As sinkhole points can be regarded as surface anomalies, the fitted surface is expected to “fail” in predicting their actual height. For “false” detections, which exhibit no anomalous surface behavior, the deviations are expected to have a relatively small predication error. To normalize the deviation error with respect to the varying sinkhole size, the mean difference, $\bar{\delta}$, is estimated

$$\bar{\delta} = \frac{\sum_{i=1}^{n}\left(z_i^{adjusted} - z_i^{measured}\right)}{n} \tag{B.3}$$

where $z_i^{adjusted}$ the adjusted surface height, $z_i^{measured}$ the original measured height, and n the number of points. For actual sinkholes, the adjusted surface should be relatively flat and the majority of points lying underneath. Candidates with mean difference close to zero either alter signs (cancels the relative difference), or have an indistinct depth relative to the surrounding surface.